Phase-evolved $BiOCl/Bi_3O_4Cl$ S-scheme Heterojunction for Enhanced Photocatalytic Nitrogen Fixation

Xitong Wang†[a], Xiao Yu†[a], Liping Feng*[a], Yuan Tian[a], Yan Li[a], Yulong Yang[a]

[a] State Key Lab of Solidification Processing, College of Materials Science and Engineering, Northwestern Polytechnical University, Xi'an, Shaanxi, 710072, People's Republic of China.

E-mail addresses: lpfeng@nwpu.edu.cn

† These authors contributed equally to this work.

Table of Contents

Methods

Theoretical calculations: The computation was performed using the VASP software based on first-principles calculation. The projected augmented wave (PAW) pseudopotential was used, and the exchange - correlation energy was treated with the PBE functional within the GGA. During geometry optimization, the cutoff energy was 500 eV, and self - consistency was achieved when the total energy converged to 10^{-5} eV/atom. The vacuum layer thickness was set to exceed 15 Å. For molecular dynamics simulations of BiOCl and Bi_3O_4Cl at 450 K, VASP was also employed. The simulation lasted 2000 fs with a 1 fs time step to evaluate thermal stability.

Photocatalytic N_2 fixation: Photocatalytic nitrogen fixation experiments were carried out in a sealed quartz reactor using a 300 W xenon lamp as the light source. First, the reactor was purged with high-purity nitrogen gas under dark conditions with continuous stirring for 30 minutes to fully saturate the reaction system with N_2. Subsequently, the photocatalytic reaction was conducted under light irradiation for 5 hours. After the reaction, 2 mL of the reaction solution was withdrawn and centrifuged to remove insoluble impurities, and the concentration of the produced ammonia was determined via the indophenol blue spectrophotometric method.

Product Detection: NH_3 concentration was determined by the indophenol blue method. To 2 mL of the reaction solution, 2 mL of a solution containing 5% salicylic acid, 5% sodium citrate and 1 M NaOH, 1 mL of 0.05 M NaClO, and 50 μL of 1% sodium nitroferricyanide dihydrate were added. After 2 hours of color development, the absorbance at 665 nm was measured by UV-Vis spectrophotometry to calculate the NH_3 yield. NO_3^- was determined by UV-Vis spectrophotometry. To 5 mL of the reaction solution, 100 μL of 0.1 M HCl and 10 μL of 0.8 wt.% ammonium sulfamate were added. After 30 min of dark incubation, the absorbance was measured to

calculate the NO_3^- concentration via A_{220}-$2A_{275}$ and a calibration curve. NO_2^- was quantified by UV-Vis spectrophotometry. To 5 mL of the reaction solution, 0.1 mL of Griess reagent (8% p-aminobenzenesulfonamide, 0.4% N-(1-naphthyl)ethylenediamine dihydrochloride) was added. After 20 min of color development, the absorbance at 540 nm was recorded to determine the NO_2^- concentration.

Supporting pictures

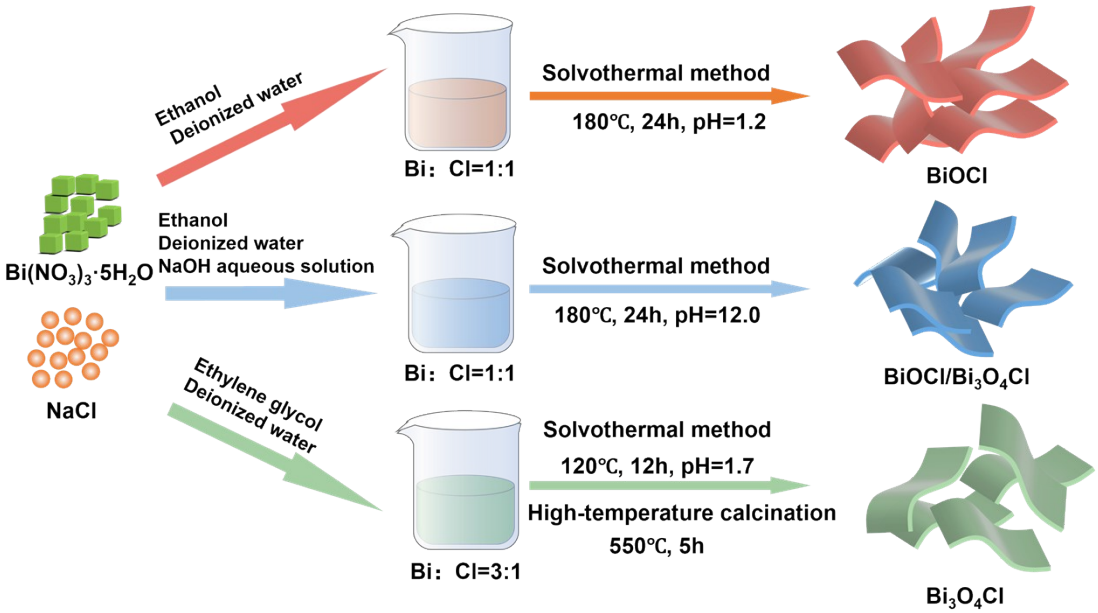

Figure S1. Schematic representation of the fabrication process of BiOCl、BiOCl/Bi_3O_4Cl and Bi_3O_4Cl

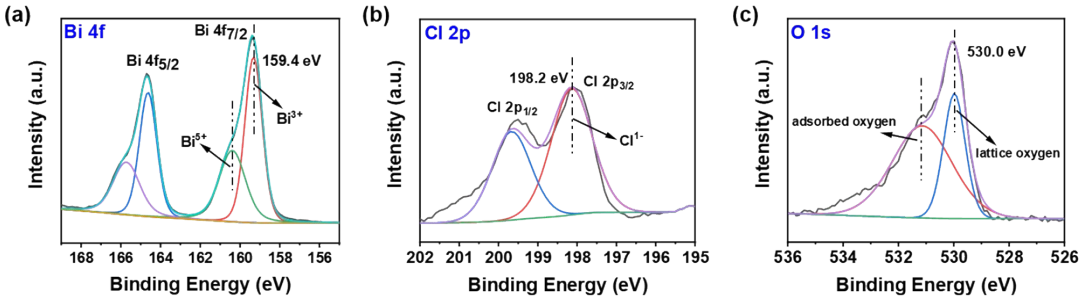

Figure S2. Bi 4f spectrum (a), Cl 2p spectrum (b) and O 1s spectrum (c) of BiOCl.

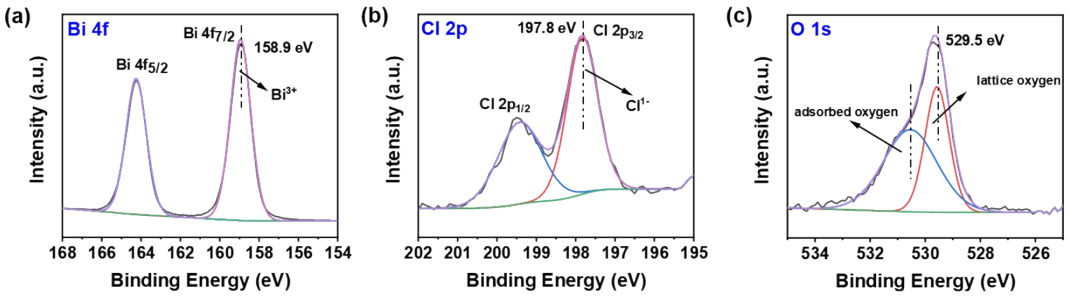

Figure S3. Bi 4f spectrum (a), Cl 2p spectrum (b) and O 1s spectrum (c) of Bi_3O_4Cl.

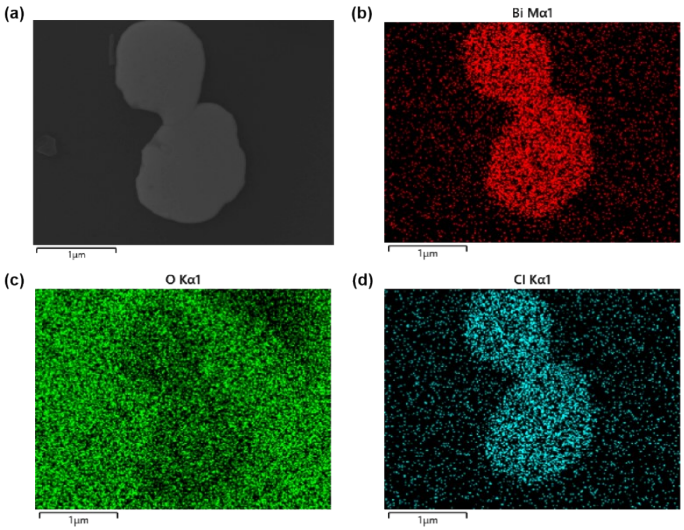

Figure S4. SEM image (a), and elemental distribution mappings Bi (b), O (c) and Cl (d) of BiOCl.

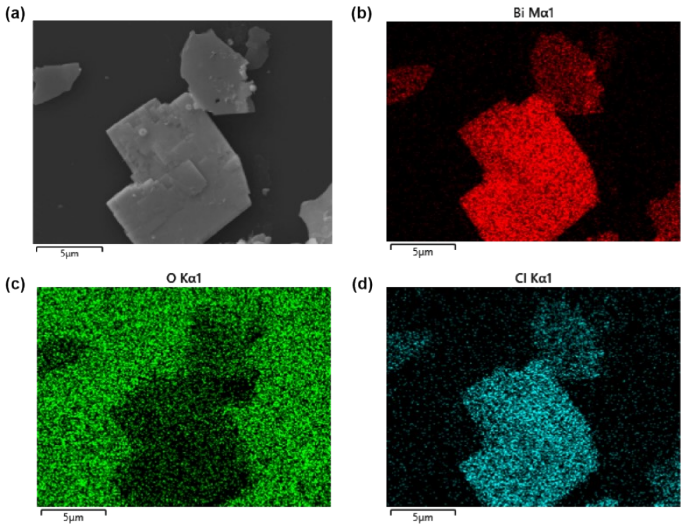

Figure S5. SEM image (a), and elemental distribution mappings Bi (b), O (c) and Cl (d) of $BiOCl/Bi_3O_4Cl$.

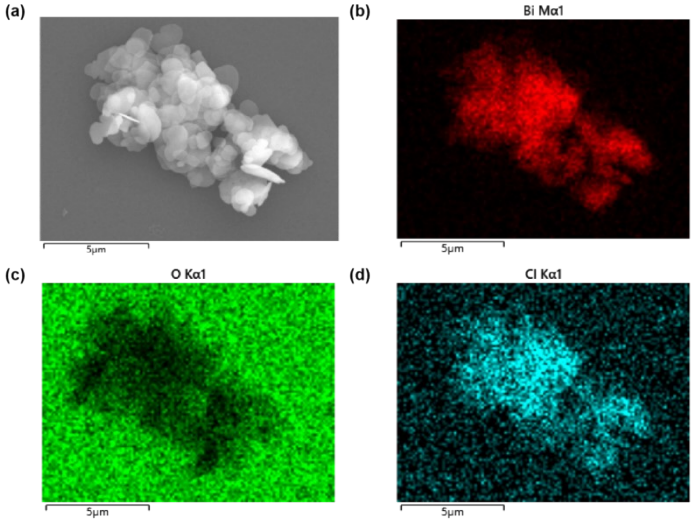

Figure S6. SEM image (a), and elemental distribution mappings Bi (b), O (c) and Cl (d) of

Bi_3O_4Cl.

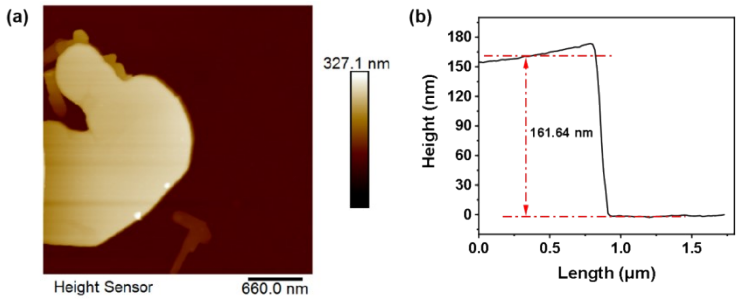

Figure S7. AFM images (a) and the corresponding height profile measured (b) of BiOCl.

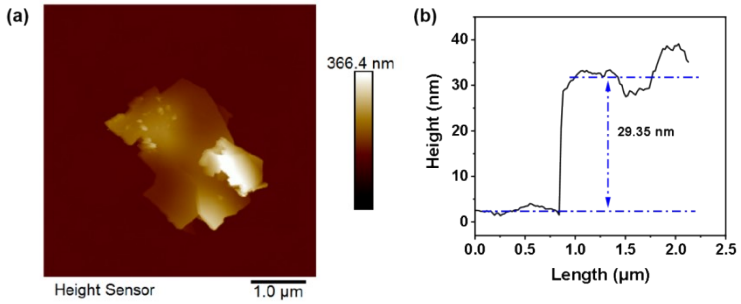

Figure S8. AFM images (a) and the corresponding height profile measured (b) of BiOCl/Bi_3O_4Cl.

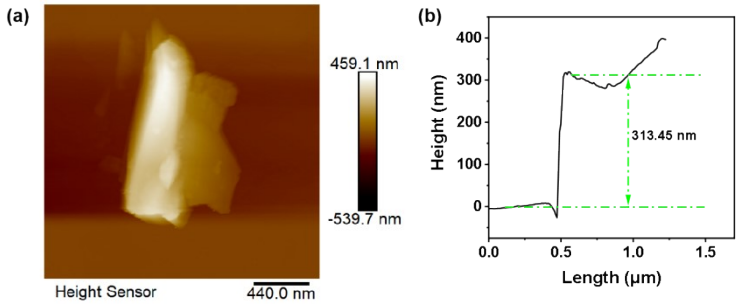

Figure S9. AFM images (a) and the corresponding height profile measured (b) of Bi_3O_4Cl.

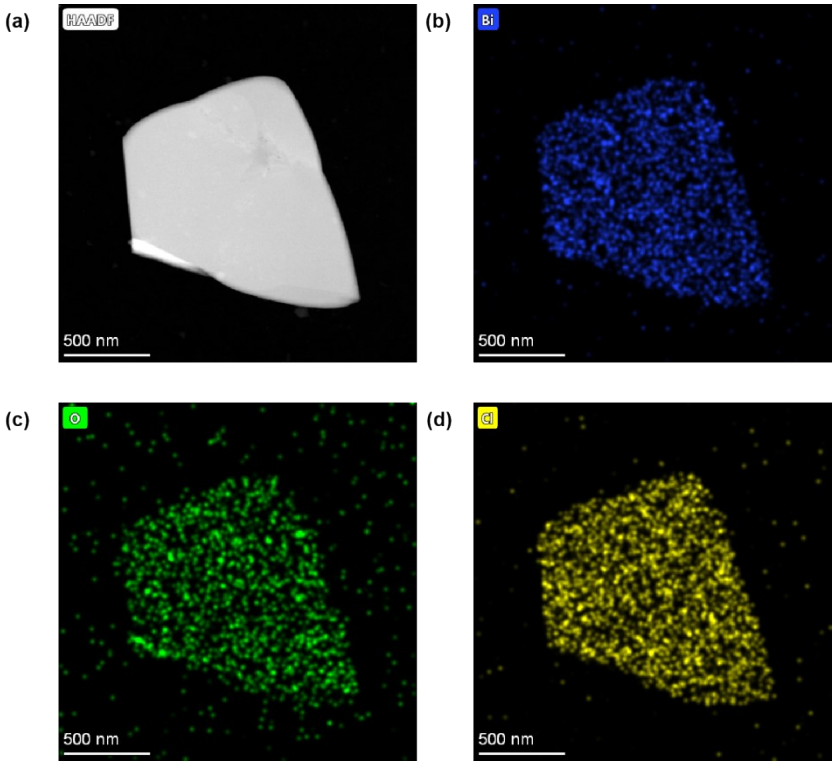

Figure S10. TEM (a), elemental distribution mappings Bi (b), O (c) and Cl (d) of BiOCl.

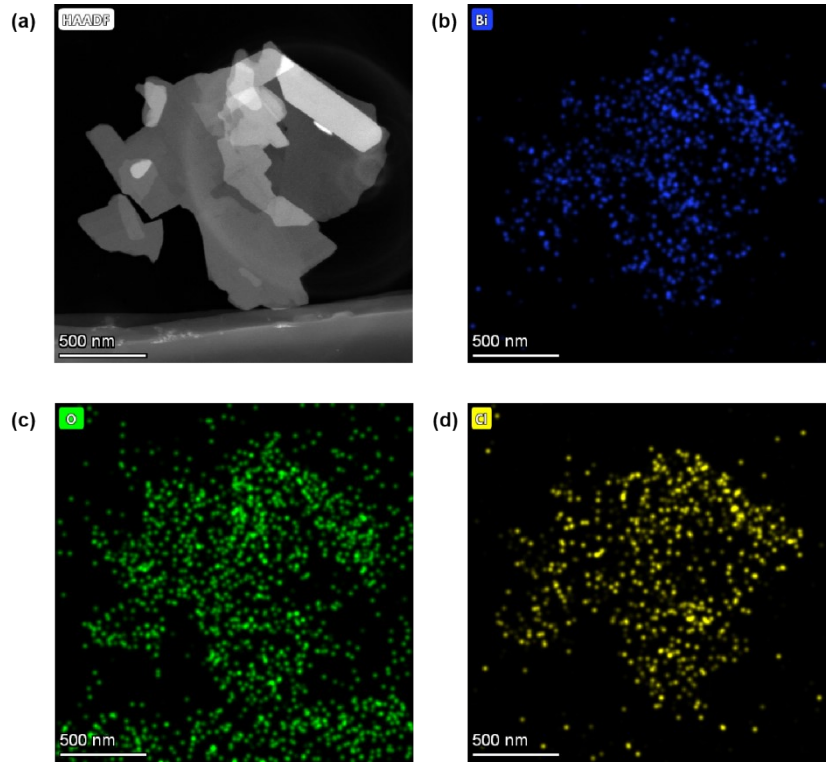

Figure S11. TEM (a), elemental distribution mappings Bi (b), O (c) and Cl (d) of Bi_3O_4Cl.

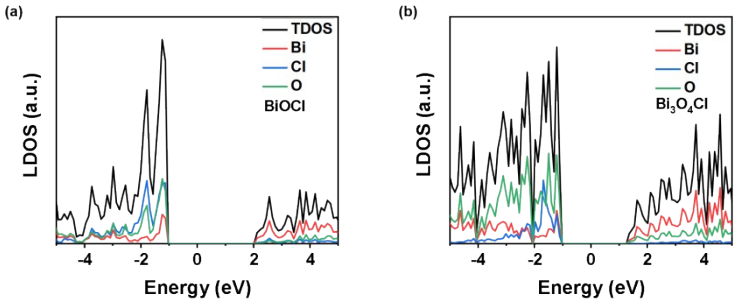

Figure S12. LDOS of BiOCl (a) and Bi_3O_4Cl (b).

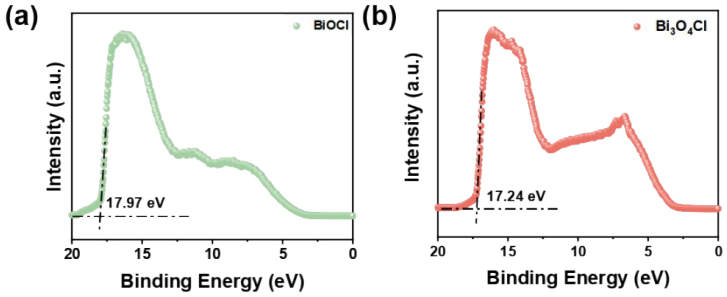

Figure S13. UPS spectra of BiOCl (a) and Bi_3O_4Cl (b).

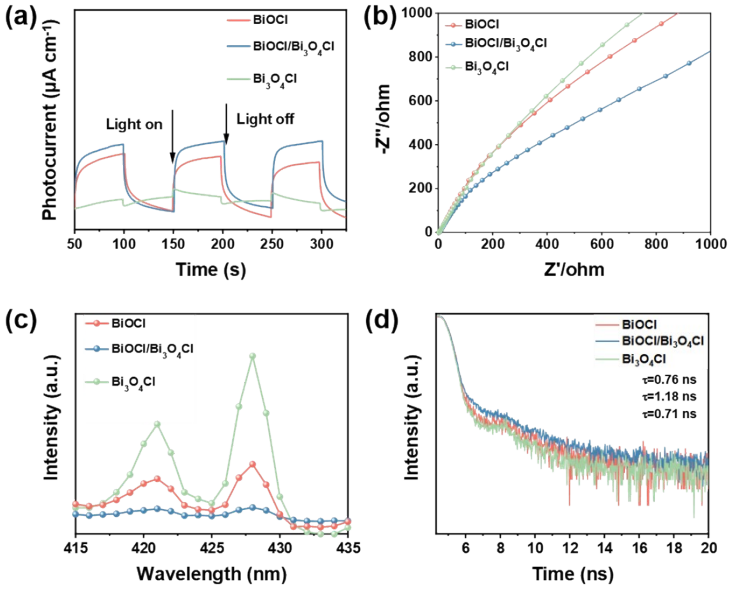

Figure S14. Transient photocurrent response (a), EIS spectrum (b), PL spectrum (c) and TRPL decay spectrum (d) of BiOCl、$BiOCl/Bi_3O_4Cl$ and Bi_3O_4Cl.

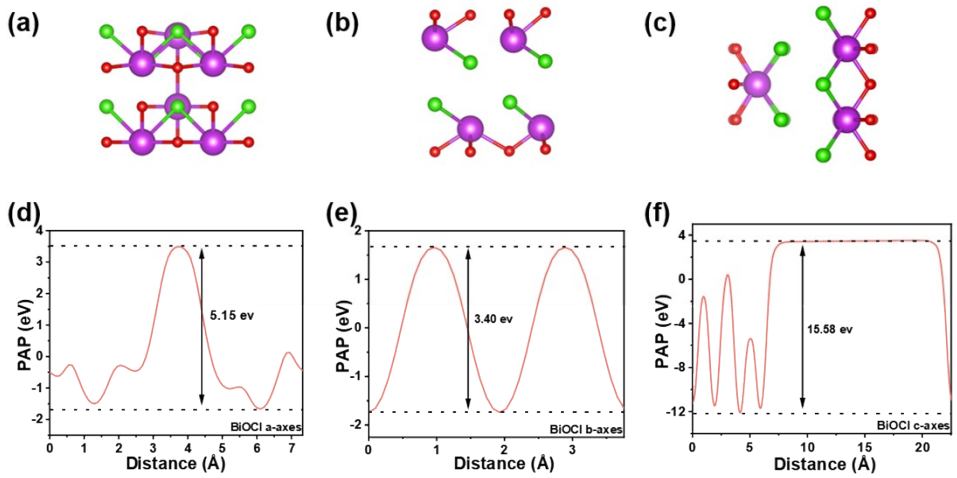

Figure S15. Schematic diagrams of BiOCl along thea-axes, b-axes, and c-axes (a-c), and planar electrostatic potentials along the three respective directions(d-f)

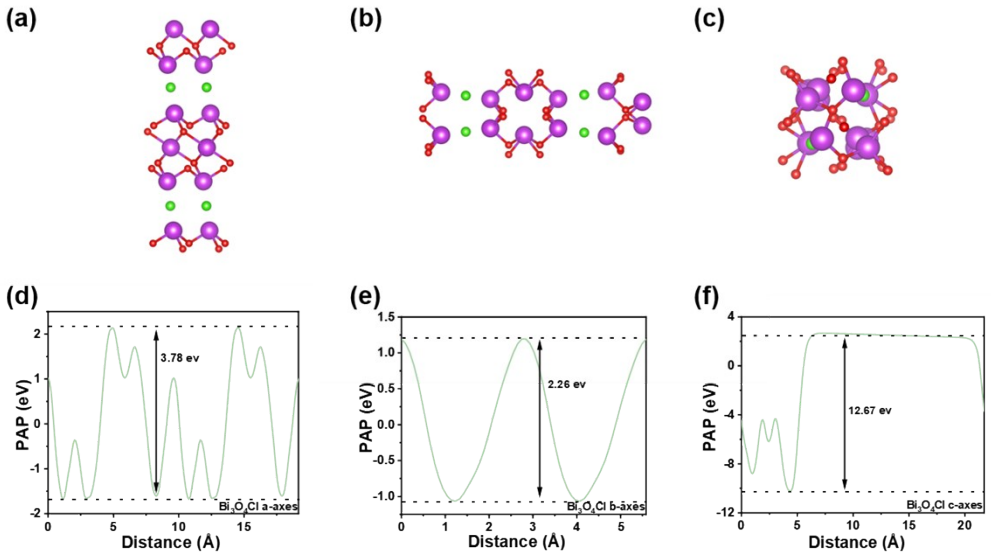

Figure S16. Schematic diagrams of Bi_3O_4Cl along thea-axes, b-axes, and c-axes (a-c), and planar electrostatic potentials along the three respective directions(d-f)

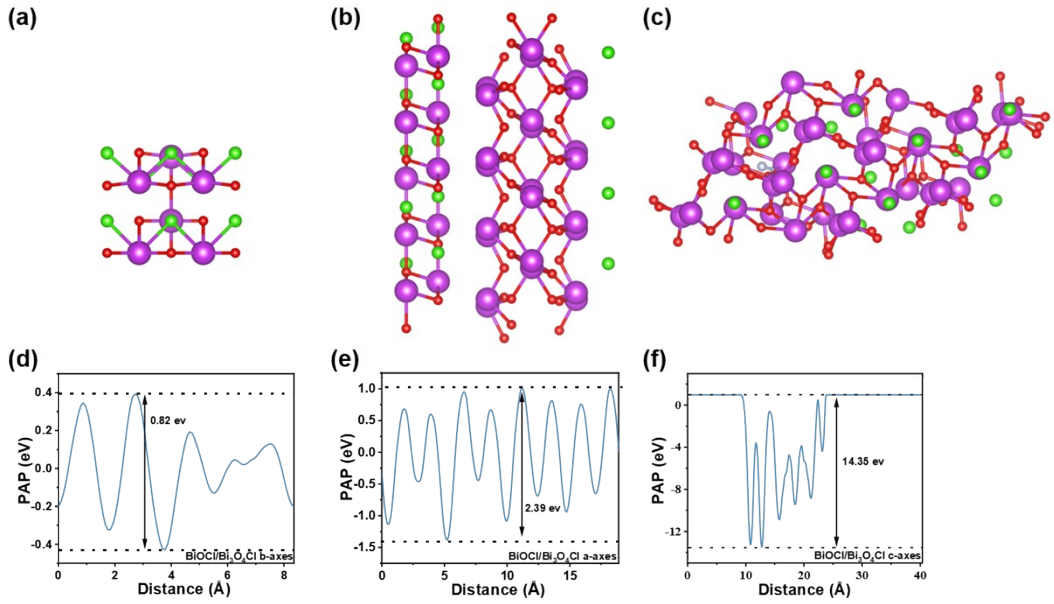

Figure S17. Schematic diagrams of $BiOCl/Bi_3O_4Cl$ along thea-axes, b-axes, and c-axes (a-c), and planar electrostatic potentials along the three respective directions(d-f)

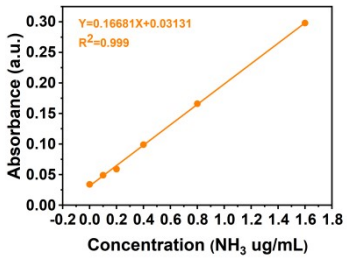

Figure S18. Standard curve for detecting ammonia with indophenol blue.

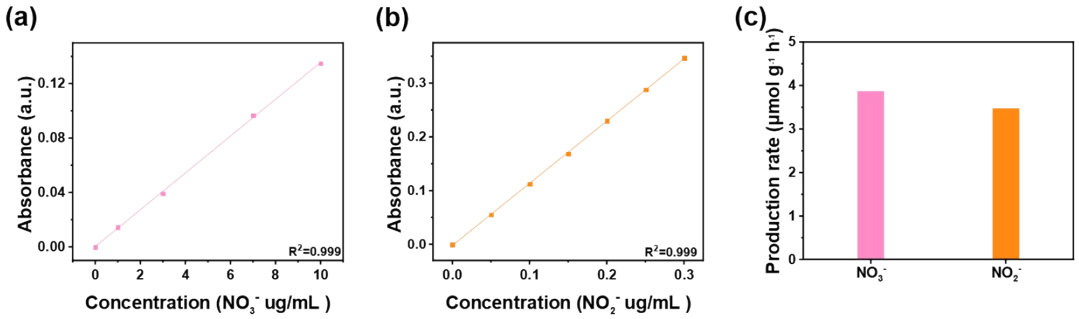

Figure S19. Standard curves of NO_3^- (a) and NO_2^- (b), and production rates of NO_3^- and NO_2^- of $BiOCl/Bi_3O_4Cl$ (c).

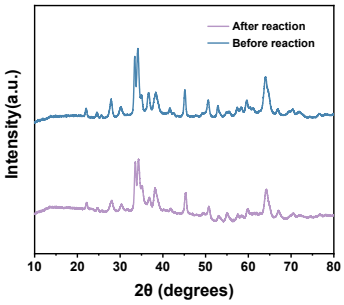

Figure S20. XRD patterns of BiOCl/Bi_3O_4Cl before and after the photocatalytic nitrogen fixation test

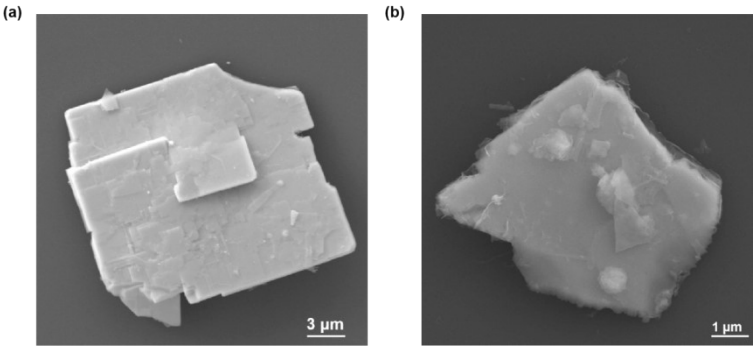

Figure S21. SEM image of BiOCl/Bi_3O_4Cl before (a) and after (b) the photocatalytic nitrogen fixation test.

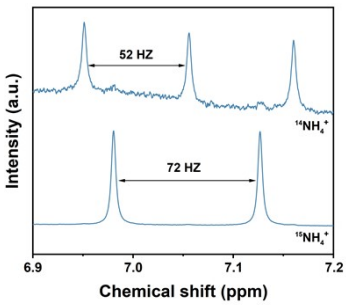

Figure S22. ^1H NMR spectrum of the product solution after the photocatalytic nitrogen fixation reaction

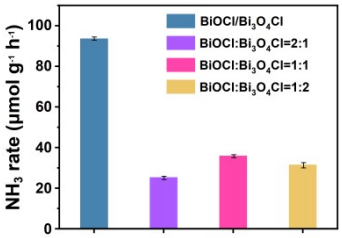

Figure S23. The NH_3 generation rate under simulated sunlight of BiOCl/Bi_3O_4Cl and direct mixing of BiOCl and Bi_3O_4Cl in different proportions

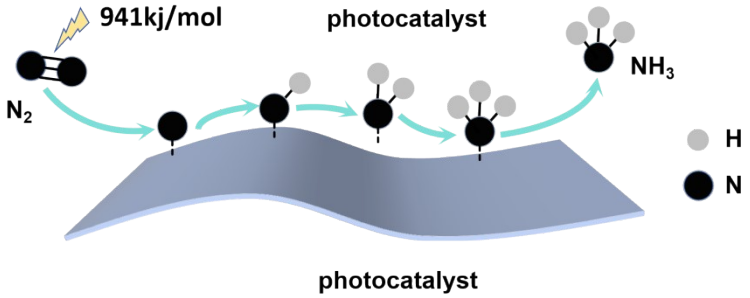

Figure S24. Schematic diagram of the direct dissociation pathway for nitrogen reduction to ammonia.

.

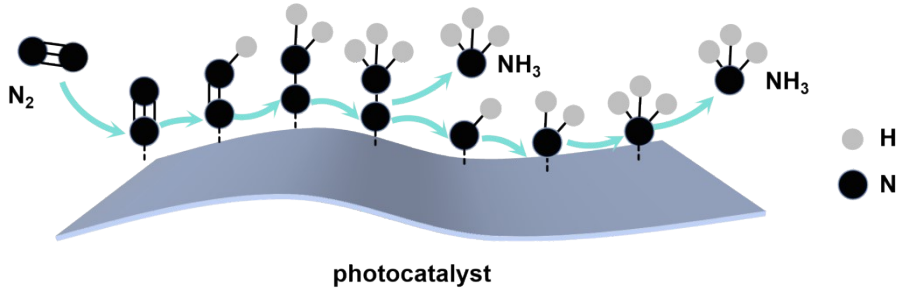

Figure S25. Schematic diagram of the of the distal dissociation pathway for nitrogen reduction to ammonia.

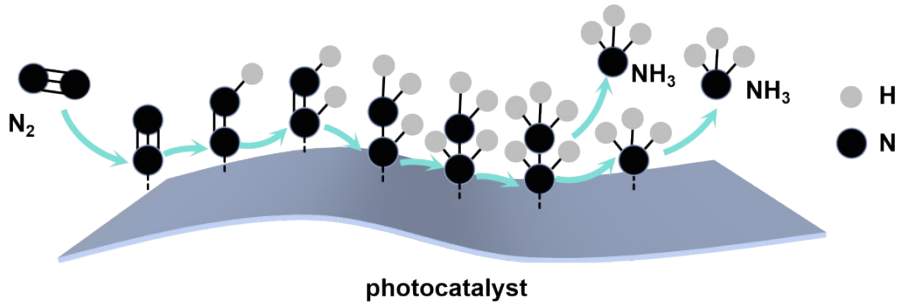

Figure S26. Schematic diagram of the of the the alternating dissociation pathway for nitrogen reduction to ammonia.

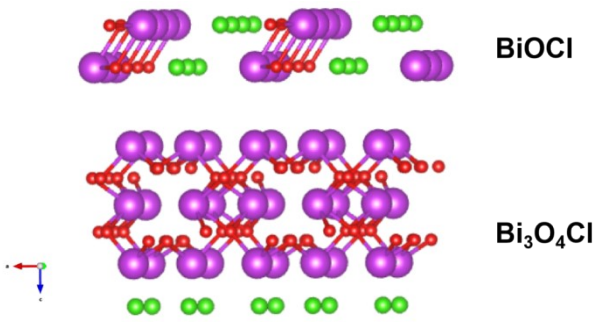

Figure S27. Schematic diagram of the $BiOCl/Bi_3O_4Cl$ heterojunction.

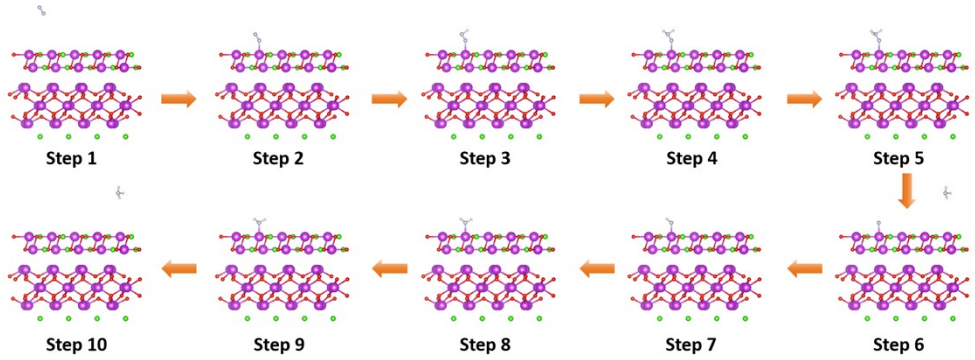

Figure S28. Schematic diagram of the nitrogen reduction structure for the distal pathway on $BiOCl/Bi_3O_4Cl$.

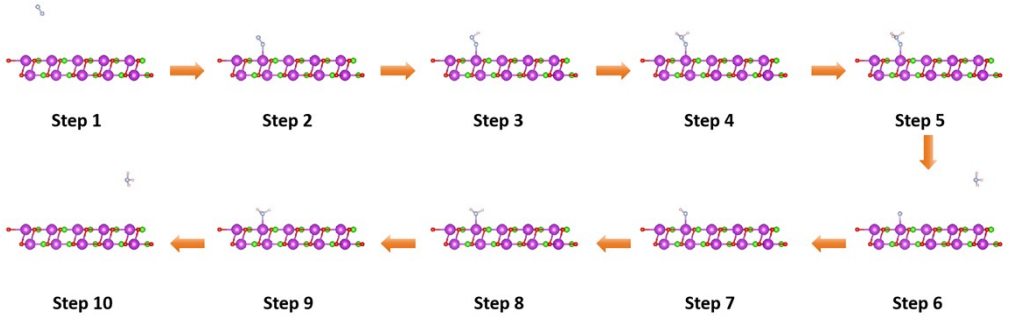

Figure S29. Schematic diagram of the nitrogen reduction structure for the distal pathway on BiOCl.

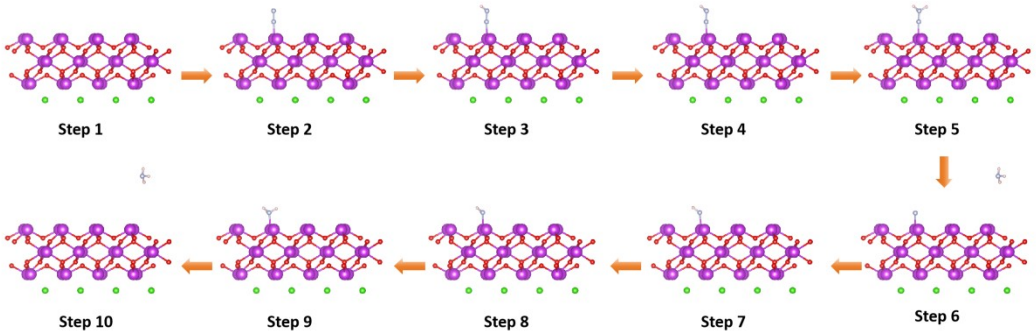

Figure S30. Schematic diagram of the nitrogen reduction structure for the distal pathway on Bi_3O_4Cl.

Figure S31. Non toxicity experiment of $BiOCl/Bi_3O_4Cl$ heterojunction

Figure S32. Growth experiment of pennywort in solution containing nitrogen reduction products (a); growth experiment of pennywort in water (b).

Supporting Tables:

Table S1 Content ratio of various elements in BiOCl.

Element	Family	Atomic Feaction (%)	Atomic Error (%)
O	K	50.59	6.13
Cl	K	24.24	8.06
Bi	L	25.27	4.69

Table S2 Content ratio of various elements in BiOCl/Bi_3O_4Cl.

Element	Family	Atomic Feaction (%)	Atomic Error (%)
O	K	67.38	13.93
Cl	K	9.98	3.83
Bi	L	22.64	4.85

Table S3 Content ratio of various elements in Bi_3O_4Cl.

Element	Family	Atomic Feaction (%)	Atomic Error (%)
O	K	78.87	9.77
Cl	K	5.84	1.57
Bi	L	15.19	2.56

TRPL spectral data fitting

TRPL is fitted by a double exponential fitting curve:

$$f(x) = A_1 e^{-i/\tau_1} + A_2 e^{-i/\tau_2} + f(x_0)$$

The average carrier lifetime is calculated as follows:

$$\tau_{average} = \frac{A_1 {\tau_1}^2 + A_2 {\tau_2}^2}{A_1 \tau_1 + A_2 \tau_2}$$

Table S4 Parameters fitted from TRPL spectra of BiOCl, BiOCl/Bi_3O_4Cl, and Bi_3O_4Cl nanosheetsb

Sample	A_1	τ_1	A_2	τ_2	$\tau_{average}$
BiOCl	89.48	0.38	10.52	3.94	0.76
BiOCl/Bi_3O_4Cl	79.18	0.39	20.80	4.30	1.18
Bi_3O_4Cl	91.00	0.37	9.00	4.18	0.71

Calculation of Apparent Quantum Yield (AQY)

The calculation formula for AQY is as follows:

$$AQY = \frac{N_e}{N_p} = \frac{10^9(\nu \times N_A \times K) \times (h \times c)}{(I \times A \times \lambda)} \times 100\%$$

Table S5 Apparent Quantum Yield at different wavelengths

Wavelength	400 nm	420 nm	450 nm	475 nm	520 nm
AQY(%)	0.176	0.117	0.052	0.023	0.029

Table S6 Comparison of catalysts for photocatalytic nitrogen fixation

Catalyst	Reaction medium	Scavenger	Light condition	Ammonia generation rate (μmol/g/h)	reference
MoO_2/BiOCl	H_2O	No	500W Xe lamp, full range light	35	[1]
Fe-BiOCl	H_2O	No	300W Xe lamp, λ=200~800 nm	30	[2]
Ce-BiOCl	H_2O	No	200W Xe lamp, full range light	46.7	[3]
r-PW12/BiOCl-OVs	H_2O	No	300W Xe lamp, full range light	33.53	[4]
OVs-$Bi_{12}O_{17}Cl_2$	H_2O	No	500W Xe lamp, λ=200~800 nm	23.43	[5]
BiOBr/BiOI/Bi	H_2O	No	300W Xe lamp, full range light	221.9	[6]
BiOBr/$Bi_4O_5Br_2$	H_2O	No	300W Xe lamp, λ＞420 nm	66.87	[7]

V_O-BiOBr	H_2O	No	300 W Xe lamp, full range light	54.70	[8]
$Bi/Bi_2Sn_2O_7$	H_2O	No	300W Xe lamp,	284.5	[9]
AgPt–TiO_2	H_2O	No	300 W Xe lamp, λ=350 nm	38.4	[10]
La-MoO_{3-x}	H_2O	No	300W Xe lamp, λ＞420 nm	209.0	[11]
MoS_2/In-Bi_2MoO_6	H_2O	No	300W Xe lamp, full range light	90	[12]
Cu-$Bi_{24}O_{31}Br_{10}$	H_2O	No	300W Xe lamp, full range light	291.1	[13]
Cu-TiO_2	H_2O	No	300W Xe lamp, full range light	78.9	[14]
V_O-Bi_5O_7I	H_2O	Ethanol	300W Xe lamp, full range light	162.48	[15]
Vo-$SrBi_4Ti_4O_{15}$	H_2O	No	300W Xe lamp, full range light	53.41	[16]
BiOCl/Bi_3O_4Cl	H_2O	No	300W Xe lamp, full range light	93.7	This work

References

1 C. Xiao, H. Wang, L. Zhang, S. Sun and W. Wang, Enhanced photocatalytic nitrogen fixation on MoO_2/BiOCl composite, *ChemCatChem*, 2019, **11**, 6467-6472.

2 Z. Shen, F. Li, J. Lu, Z. Wang, R. Li, X. Zhang, C. Zhang, Y. Wang, Y. Wang, Z. Lv, J. Liu and C. Fan, Enhanced N_2 photofixation activity of flower-like BiOCl by in situ Fe(iii) doped as an activation center, *J. Colloid. Interface. Sci.*, 2021, **584**, 174-181.

3 H. Li, J. Wang, Z. Ruan, P. Nan, B. Ge, M. Cheng, L. Yang, X. Li, Q. Liu, B. Pan, Q. Zhang, C. Xiao and Y. Xie, Electron transfer bridge inducing polarization of nitrogen molecules for enhanced photocatalytic nitrogen fixation, *Mater. Horiz.*, 2023, **10**, 5053-5059.

4 M. Sun, R. Zhang, A. Sun, X. Jia, X. Liu, X. Yu and Y. Xing, Heteropoly blue-modified ultrathin bismuth oxychloride nanosheets with oxygen vacancies for efficient photocatalytic nitrogen fixation in pure water, *J. Colloid. Interface. Sci.*, 2025, **677**, 610-619.

5 S. H. W. Kok, J. Lee, W. Chong, B. Ng, X. Y. Kong, W. Ong, S. Chai and L. Tan, Bismuth-rich $Bi_{12}O_{17}Cl_2$ nanorods engineered with oxygen vacancy defects for enhanced photocatalytic nitrogen fixation, *J. Alloy. Compd.*, 2023, **952**, 170015.

6 K. Gao, H. Zhu, C. Zhang, X. Song, L. Lao, L. Ni, J. Chen, C. Cheng and X. Wang, Boosting photocatalytic nitrogen fixation via in situ constructing Bi metal active sites over BiOBr/BiOI heterojunction, *Sol. RRL*, 2022, **6**, 2200869.

7 H. Wang, Z. Chen, Y. Shang, C. Lv, X. Zhang, F. Li, Q. Huang, X. Liu, W. Liu, L. Zhao, L. Ye, H. Xie and X. Jin, Boosting carrier separation on a BiOBr/$Bi_4O_5Br_2$ direct Z-scheme heterojunction for superior photocatalytic nitrogen fixation, *ACS Catal.*, 2024, **14**, 5779-5787.

8 X. Xue, R. Chen, H. Chen, Y. Hu, Q. Ding, Z. Liu, L. Ma, G. Zhu, W. Zhang, Q. Yu, J. Liu, J. Ma and Z. Jin, Oxygen vacancy engineering promoted photocatalytic ammonia synthesis on ultrathin two-dimensional bismuth oxybromide nanosheets, *Nano Lett.*, 2018, **18**, 7372-7377.

9 R. Wu, S. Gao, C. Jones, M. Sun, M. Guo, R. Tai, S. Chen and Q. Wang, Bi/BSO heterojunctions via vacancy engineering for efficient photocatalytic nitrogen fixation, *Adv. Funct. Mater.*, 2024, **34**, 2314051.

10 X. Bian, Y. Zhao, S. Zhang, D. Li, R. Shi, C. Zhou, L. Wu and T. Zhang, Enhancing the supply of activated hydrogen to promote photocatalytic nitrogen fixation, *ACS Mater. Lett.*, 2021, **3**, 1521-1527.

11 X. Liu, Y. Luo, C. Ling, Y. Shi, G. Zhan, H. Li, H. Gu, K. Wei, F. Guo, Z. Ai and L. Zhang, Rare earth La single atoms supported MoO_{3-x} for efficient photocatalytic nitrogen fixation, *Applied Catalysis B: Environmental*, 2022, **301**, 120766.

12 T. Ma, R. Li, Y. Huang, Y. Lu, L. Guo, M. Niu, X. Huang, R. A. Soomro, J. Ren, Q. Wang, B. Xu, C. Yang, F. Fu and D. Wang, Interfacial chemical-bonded MoS_2/In–Bi_2MoO_6 heterostructure for enhanced photocatalytic nitrogen-to-ammonia conversion, *ACS Catal.*, 2024, **14**, 6292-6304.

13 J. Di, C. Chen, Y. Wu, Y. Zhao, C. Zhu, Y. Zhang, C. Wang, H. Chen, J. Xiong, M. Xu, J. Xia, J. Zhou, Y. Weng, L. Song, S. Li, W. Jiang and Z. Liu, Polarized Cu–Bi site pairs for non-covalent to covalent interaction tuning toward N_2 photoreduction, *Adv. Mater.*, 2022, **34**, 2204959.

14 Y. Zhao, Y. Zhao, R. Shi, B. Wang, G. I. N. Waterhouse, L. Wu, C. Tung and T. Zhang, Tuning oxygen vacancies in ultrathin TiO_2 nanosheets to boost photocatalytic nitrogen fixation up to 700 nm, *Adv. Mater.*, 2019, **31**, 1806482.

15 M. Lan, N. Zheng, X. Dong, C. Hua, H. Ma and X. Zhang, Bismuth-rich bismuth oxyiodide microspheres with abundant oxygen vacancies as an efficient photocatalyst for nitrogen fixation, *Dalton Trans.*, 2020, **49**, 9123-9129.

16 S. Gao, H. Ji, P. Yang, M. Guo, J. Tressel, S. Chen and Q. Wang, High-performance photocatalytic reduction of nitrogen to ammonia driven by oxygen vacancy and ferroelectric polarization field of $SrBi_4Ti_4O_{15}$ nanosheets, *Small*, 2023, **19**, 2206114.